

# In Silico, in Vitro, and in Vivo Evaluation of New Candidates for $\alpha$ -Synuclein PET Imaging

Mathieu Verdurand,<sup>†,#</sup> Elise Levigoureux,<sup>\*,†,‡,#</sup> Wael Zeinyeh,<sup>†</sup> Laurent Berthier,<sup>||</sup> Meriem Mendjel-Herda,<sup>†</sup> Florence Cadarossanesaib,<sup>§</sup> Caroline Bouillot,<sup>§</sup> Thibault Jecker,<sup>§</sup> Raphaël Terreux,<sup>||</sup> Sophie Lancelot,<sup>†,‡</sup> Fabien Chauveau,<sup>†</sup> Thierry Billard,<sup>§,⊥</sup> and Luc Zimmer<sup>†,‡,§</sup>

<sup>†</sup>Université de Lyon, Université Claude Bernard Lyon 1, Lyon Neuroscience Research Center, CNRS UMR5292, INSERM U1028, Lyon 69361, France

<sup>‡</sup>Hospices Civils de Lyon, Lyon 69361, France

<sup>§</sup>CERMEP-Imaging Platform, Bron 69677, France

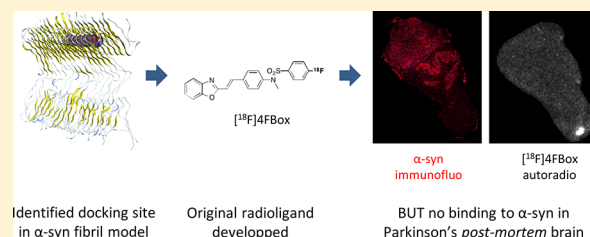
<sup>⊥</sup>Université de Lyon, Université Claude Bernard Lyon 1, Institute of Chemistry and Biochemistry, CNRS UMR5246, Villeurbanne 69100, France

<sup>||</sup>Université de Lyon, Université Claude Bernard Lyon 1, Institute of Biology and Chemistry of Proteins, CNRS UMR5305, Lyon 69361, France

## Supporting Information

**ABSTRACT:** Accumulation of  $\alpha$ -synuclein ( $\alpha$ -syn) is a neuro-pathological hallmark of synucleinopathies. To date, no selective  $\alpha$ -syn positron emission tomography (PET) radiotracer has been identified. Our objective was to develop the first original, selective, and specific  $\alpha$ -syn PET radiotracer. Chemical design inspired from three structural families that demonstrated interesting  $\alpha$ -syn binding characteristics was used as a starting point. Bioinformatics modeling of  $\alpha$ -syn fibrils was then employed to select the best molecular candidates before their syntheses. An *in vitro* binding assay was performed to evaluate the affinity of the compounds. Radiotracer specificity and selectivity were assessed by *in vitro* autoradiography and *in vivo* PET studies in animal (rodents) models. Finally, gold standard *in vitro* autoradiography with patients' postmortem tissues was performed to confirm/infirm the  $\alpha$ -syn binding characteristics. Two compounds exhibited a good brain availability and bound to  $\alpha$ -syn and A $\beta$  fibrils in a rat model. In contrast, no signal was observed in a mouse model of synucleinopathy. Experiments in human tissues confirmed these negative results.

**KEYWORDS:** synucleinopathies, Parkinson's disease, multiple system atrophy,  $\alpha$ -synuclein, radiotracer, positron emission tomography



## INTRODUCTION

Several neurodegenerative diseases share common pathological mechanisms, whereby certain endogenous proteins (amyloid- $\beta$  or A $\beta$ ,  $\alpha$ -synuclein or  $\alpha$ -syn, Tau protein or  $\tau$ ) form fibrillary aggregates composed of  $\beta$ -sheet structures that are linked with the pathological processes.<sup>1</sup> Among neurodegenerative protei-nopathies, those characterized by  $\alpha$ -syn protein aggregates form a heterogeneous group of diseases called “synucleinopathies”.  $\alpha$ -synuclein aggregates are localized inside neurons in Parkinson's disease (PD), PD with dementia (PDD), and dementia with Lewy bodies (DLB), while they form oligodendroglial cytoplasmic inclusions in multiple system atrophy (MSA).<sup>2</sup>

International guidelines have highlighted a crucial need to develop tools for brain imaging in the diagnosis and follow-up of these diseases.<sup>3–5</sup> Positron emission tomography (PET) enables noninvasive *in vivo* and *in situ* visualization, characterization, and quantification of physiological processes at the cellular or molecular level. In the absence of early clinically

relevant biomarkers, PET imaging of  $\alpha$ -syn would allow better understanding of pathophysiological processes involving  $\alpha$ -syn, differential and possibly presymptomatic diagnosis of synucleinopathies and, finally, evaluation of disease-modifying drugs targeting  $\alpha$ -syn.<sup>6</sup>

The development of a radiopharmaceutical specifically binding to  $\alpha$ -syn aggregates raises numerous challenges. First, in terms of sensitivity, as  $\alpha$ -syn aggregates are present at lower density than A $\beta$  aggregates *in vivo*. Second, in terms of localization, as  $\alpha$ -syn aggregates are localized intracellularly and thus need a radiotracer able to cross the blood brain barrier (BBB) and, neuron or oligodendrocyte membranes. Last but not least, a successful radiotracer will have to be selective against the other proteins that also form  $\beta$ -sheets 3-

**Received:** March 2, 2018

**Revised:** May 29, 2018

**Accepted:** July 10, 2018

**Published:** July 10, 2018

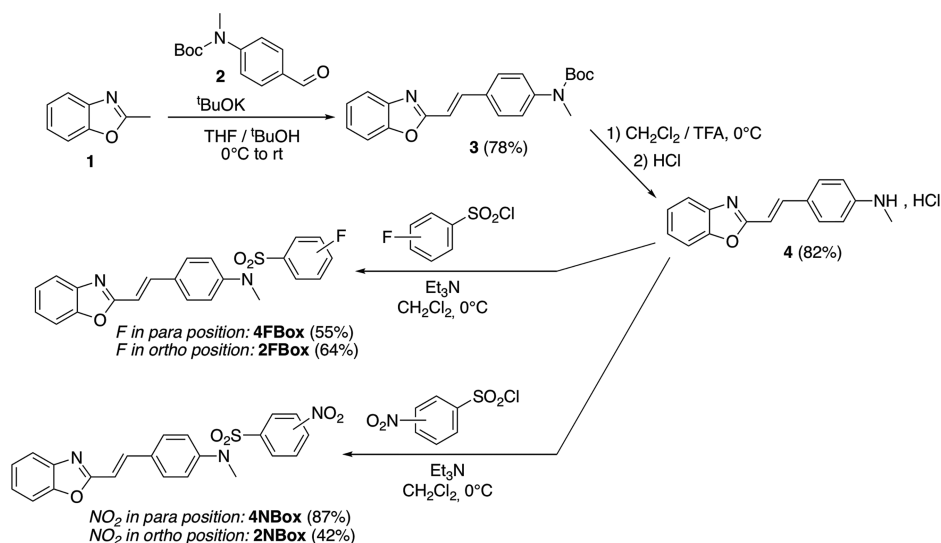


**Figure 1.** Diagram of the chemical syntheses of the nonradioactive FBox compounds and their precursors (Nbox) for radiosyntheses.

dimensional (3D) structures:  $A\beta$ ,  $\tau$ , TDP-43, and insulin. The most noticeable are  $A\beta$  aggregates, found in Alzheimer's disease (AD) but also in other neurodegenerative diseases, including synucleinopathies.<sup>7,8</sup> Concurrently, the majority of DLB patients exhibit extensive cortical  $A\beta$  deposition.<sup>9</sup> This overlap complicates the quantification of PET images, pushing the PET imaging community to investigate, in depth, the precise selectivity of the radiotracers already developed and of those to come. In this regard, a particularly important and difficult point is to find one or several models (cell lines overexpressing  $\alpha$ -syn, *in vitro*  $\alpha$ -syn fibrils, transgenic animals overexpressing  $\alpha$ -syn) that accurately reflect the aggregation process occurring in humans,<sup>10</sup> knowing that the gold-standard will always be the evaluation performed on human tissue and, ultimately, *in vivo* in patients.

All of these challenges can explain that there is still no PET radiotracer available to measure the  $\alpha$ -syn protein brain accumulation. If the amyloid radioligand 5-[(*E*)-2-[6-(2-[<sup>18</sup>F]fluoroethoxy)-1,3-benzoxazol-2-yl]ethenyl]-*N,N*-dimethyl-1,3-thiazol-2-amine (BF227), radiolabeled with <sup>11</sup>C or <sup>18</sup>F, has demonstrated interesting binding properties to fibrils *in vitro*<sup>11</sup> and  $\alpha$ -syn glial inclusions in MSA patients,<sup>12</sup> these results have not been extended to  $\alpha$ -syn accumulation in other synucleinopathies, such as PD, PDD, or DLB. Other lead compounds, such as [<sup>125</sup>I]SIL23, that binds selectively to  $\alpha$ -syn *in vitro*,<sup>13</sup> or [<sup>18</sup>F]46a, with a selectivity for  $\alpha$ -syn recombinant fibrils higher than that for  $A\beta$  fibrils,<sup>14</sup> all failed *in vivo*.

The aim of this study was thus to develop a PET radiotracer of aggregated  $\alpha$ -syn proteins. The present study followed a rational and multidisciplinary approach to orient the design and the evaluation of  $\alpha$ -syn PET radiotracer-candidates. Several steps were undertaken with, first, the chemical design of candidate molecules derived from three structural families that demonstrated interesting  $\alpha$ -syn binding characteristics in the literature.<sup>11,15–18</sup> The second step used bioinformatics modeling tools to model an  $\alpha$ -syn fibril, propose an interesting docking site along the fibril, and evaluate the docking capabilities of our candidates toward this interaction site and also their ability to reach the identified binding pocket. As a final step, the “best” candidates were synthesized, radiolabeled with <sup>18</sup>F, tested *in vitro*, and evaluated by *in vitro/in vivo*

imaging studies in several animal models and, ultimately, *postmortem* on AD, PD, and MSA patients' brains.

## ■ MATERIALS AND METHODS

### Computational Studies. Modelization of $\alpha$ -syn Fibrils.

The sequence of  $\alpha$ -syn was obtained from the UniProt database. Using the Protein Data Bank structure 2MPZ as a scaffold,<sup>19</sup> modifications were made to replace the amino acids by the  $\alpha$ -syn sequence. The resulting layer model was duplicated on the fibril axes, following  $\beta$ -pleated conformation determined from a cryo-electron microscopy map (EMD-6482),<sup>20</sup> to obtain a final model composed of 18 layers. After energy minimization, the structure was processed in a 20 ns molecular dynamics simulation.

**Identification of a Docking Site.** Simulations were performed with AMBER software version 16. All simulations were performed in the conditions of a solution, using 5-site transferable interaction potential (TIP3P) as the water model, and the system was neutralized with chloride ions ( $\text{Cl}^-$ ). The periodic boundary condition was chosen as a parallelepiped with about a 12 Å extension in all directions. The molecular simulation time step was set at 2 fs, with 300 K as the final temperature and 1 atm as the pressure, leading to the discrimination of different conformations. The binding sites were identified for these fibril structures, using the Site Finder program implemented in the molecular operating environment (MOE).

**Evaluation of Docking Performance.** All docking scores were performed with MOE 2014 in the interaction site determined using Site Finder, and the best conformations of the complex were transferred to umbrella sampling simulations.

**Ability To Reach the Identified Docking Site.** Umbrella sampling simulations were performed with 220 windows, with distances between the center of mass of the tracer and the atoms of the protein ranging from 27 to 5.1 Å at 0.1 Å intervals. In each window, a harmonic potential with a 25 kcal/mol·Å<sup>2</sup> force constant was applied to maintain these previous distances. Also, positional restraints were applied to the backbone atoms of the two proteins, which were at the edge of the fibril, and the atoms of the protein concerned by the reaction coordinate. For each window, we performed a

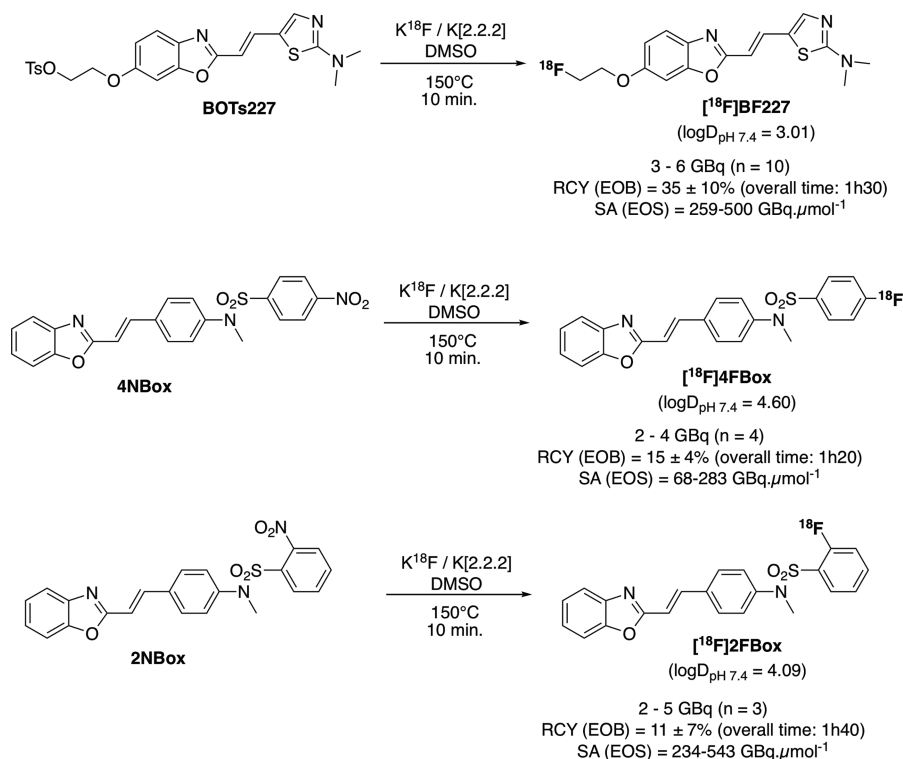


**Figure 2.** Diagram of the radiosynthesis of [ $^{18}F$ ]BF227 (A), [ $^{18}F$ ]4FBox (B), and [ $^{18}F$ ]2FBox (C). RCY data are mean  $\pm$  SD values.

simulation of 40 ps duration for equilibration and 100 ps duration for production, with data collection every 50 fs at 300 K and 1 atm. Finally, the weighted histogram analysis method was employed to reconstruct the free energy profile along the reaction coordinate from the biased probability distribution of each window.

**Chemical Syntheses.** These syntheses are shown in (Figure 1).

**Synthesis of tert-Butyl N-{4-[(E)-2-(1,3-Benzoxazol-2-yl)ethenyl]phenyl}-N-methylcarbamate (3).** To a solution of **1** (0.435 mL, 3.70 mmol) and **2** (0.725 g, 3.08 mmol) in THF/tert-butanol (30 mL/1.8 mL), cooled at  $0^{\circ}C$ , was added potassium *tert*-butoxide (0.442 g, 4.01 mmol). After 1 h at  $0^{\circ}C$ , the reacting mixture was stirred overnight at room temperature. Then, a saturated aqueous solution of  $NaHCO_3$  was added, followed by extraction with ethyl acetate. The organic phase was then washed with brine and dried over  $MgSO_4$ . After evaporation, purification by flash chromatography (eluent: pentane/ethyl acetate, 90:10) was performed to obtain **3**, as a yellow solid (0.843 g, 78%).

$^1H$  NMR ( $CDCl_3$ , 300 MHz),  $\delta$ : 7.86 (d, 1H,  $J = 16.2$  Hz), 7.80–7.70 (m, 1H), 7.62–7.51 (m, 3H), 7.40–7.28 (m, 4H), 7.08 (d, 1H,  $J = 16.2$  Hz), 3.30 (s, 3H), 1.48 (s, 9H).

**Synthesis of 4-[(E)-2-(1,3-Benzoxazol-2-yl)ethenyl]-N-methylaniline Hydrochloride (4).** To a solution of **3** (0.82g, 2.34 mmol) in  $CH_2Cl_2$  (19 mL), cooled at  $0^{\circ}C$ , was added trifluoroacetic acid (1.9 mL). The solution was stirred at  $0^{\circ}C$  for 4 h, the solvents were evaporated in vacuo, and the resulting mixture was extracted with ethyl acetate and saturated aqueous solution of  $NaHCO_3$ . The organic phase was washed with brine and dried over  $Na_2SO_4$ . After evaporation, THF and HCl (37%) were added. The precipitated solid was filtered and washed with THF. All of the resulting organic phases were neutralized with a saturated aqueous solution of  $NaHCO_3$ . After evaporation, the resulting mixture was then extracted

with ethyl acetate. The organic phase was then evaporated, and HCl (37%) was added to form another precipitate. All of the obtained solids were combined to afford **4** as a yellow solid (0.551 g, 82%).

$^1H$  NMR ( $CD_3OD$ , 300 MHz),  $\delta$ : 7.93–7.81 (m, 3H), 7.73–7.60 (m, 2H), 7.49–7.35 (m, 4H), 7.21 (d, 1H,  $J = 16.3$  Hz), 3.07 (s, 3H).

**Synthesis of N-{4-[(E)-2-(1,3-Benzoxazol-2-yl)ethenyl]phenyl}-4-fluoro-N-methylbenzene-1-sulfonamide (4FBox).** To a solution of **4** (0.128 g, 0.45 mmol) and 4-fluorobenzenesulfonyl chloride (0.088 g, 0.45 mmol) in anhydrous  $CH_2Cl_2$  (7 mL), cooled at  $0^{\circ}C$ , was added trimethylamine (0.155 mL, 1.12 mmol). The reacting mixture was then stirred at room temperature for 24 h. After evaporation of the solvents, the resulting mixture was dissolved with  $CH_2Cl_2$  and washed with an aqueous solution of  $KHSO_4$  (5%) and then with brine. After purification with flash chromatography ( $CH_2Cl_2$ /diethyl ether), **4FBox** (0.1 g, 55%) was obtained as a yellow solid.

$^1H$  NMR ( $DMSO-d_6$ , 400 MHz),  $\delta$ : 7.84–7.77 (m, 3H), 7.76–7.69 (m, 2H), 7.63–7.57 (m, 2H), 7.47–7.35 (m, 4H), 7.33 (d, 1H,  $J = 16.4$  Hz), 7.23–7.18 (m, 2H), 3.17 (s, 3H).  $^{13}C$  NMR ( $DMSO-d_6$ , 100 MHz),  $\delta$ : 164.7 (d,  $J = 252$  Hz), 162.6, 149.8, 142.0, 141.7, 138.3, 133.6, 132.1 (d,  $J = 2.7$  Hz), 130.5 (d,  $J = 9.8$  Hz), 128.5, 126.2, 125.6, 124.8, 119.6, 116.6 (d,  $J = 23.0$  Hz), 114.4, 110.6, 37.6.  $^{19}F$  NMR ( $DMSO-d_6$ , 282 MHz),  $\delta$ : –105.91.

**Synthesis of N-{4-[(E)-2-(1,3-Benzoxazol-2-yl)ethenyl]phenyl}-2-fluoro-N-methylbenzene-1-sulfonamide (2FBox).** A similar procedure to **4FBox** with 2-fluorobenzenesulfonyl chloride was used. **2FBox** was obtained as a yellow solid (0.1 g, 64%).

$^1H$  NMR ( $DMSO-d_6$ , 400 MHz),  $\delta$ : 7.83–7.63 (m, 7H), 7.51–7.25 (m, 7H), 3.29 (d,  $J = 1.3$  Hz, 3H).  $^{13}C$  NMR

(DMSO- $d_6$ , 100 MHz),  $\delta$ : 162.3, 158.1 (d,  $J = 254.9$  Hz), 149.8, 141.69, 141.65, 138.3, 136.3 (d,  $J = 8.6$  Hz), 133.5, 130.9, 128.5, 125.9, 125.6, 125.1 (d,  $J = 3.6$  Hz), 124.8, 124.6 (d,  $J = 14.6$  Hz), 119.6, 117.6 (d,  $J = 21.5$  Hz), 114.3, 110.6, 37.6 (d,  $J = 2.8$  Hz).  $^{19}\text{F}$  NMR (DMSO- $d_6$ , 282 MHz),  $\delta$ : -108.61.

**Synthesis of *N*-{4-[(*E*)-2-(1,3-Benzoxazol-2-yl)ethenyl]-phenyl}-*N*-methyl-4-nitrobenzene-1-sulfonamide (4NBox).** A similar procedure to 4FBox with 4-nitrobenzenesulfonyl chloride was used. 4NBox was obtained as a yellow solid (0.145 g, 87%).

$^1\text{H}$  NMR (DMSO- $d_6$ , 400 MHz),  $\delta$ : 8.43–8.37 (m, 2H), 7.85–7.78 (m, 5H), 7.76–7.70 (m, 2H), 7.44–7.38 (m, 2H), 7.35 (d, 1H,  $J = 16.4$  Hz), 7.25–7.21 (m, 2H), 3.23 (s, 3H).  $^{13}\text{C}$  NMR (DMSO- $d_6$ , 100 MHz),  $\delta$ : 162.2, 150.1, 149.8, 141.7, 141.5, 141.2, 138.3, 134.0, 129.0, 128.6, 126.6, 125.6, 124.8, 124.6, 119.7, 114.6, 110.6, 37.9.

**Synthesis of *N*-{4-[(*E*)-2-(1,3-Benzoxazol-2-yl)ethenyl]-phenyl}-*N*-methyl-2-nitrobenzene-1-sulfonamide (2NBox).** A similar procedure to 4FBox with 2-nitrobenzenesulfonyl chloride was used. 2NBox was obtained as a yellow solid (0.07 g, 42%).

$^1\text{H}$  NMR (DMSO- $d_6$ , 400 MHz),  $\delta$ : 8.00 (dd,  $J = 8.0$  Hz, 1.1 Hz, 1H), 7.92 (td,  $J = 7.7$  Hz, 1.1 Hz, 1H), 7.88–7.68 (m, 7H), 7.45–7.29 (m, 5H), 3.33 (s, 3H).  $^{13}\text{C}$  NMR (DMSO- $d_6$ , 100 MHz),  $\delta$ : 162.2, 149.8, 147.9, 141.7, 141.2, 138.3, 135.2, 134.0, 132.3, 130.4, 129.0, 128.7, 126.7, 125.6, 124.8, 124.3, 119.7, 114.6, 110.6, 38.4.

**Radiolabeling of [ $^{18}\text{F}$ ]BF227, [ $^{18}\text{F}$ ]2FBox, and [ $^{18}\text{F}$ ]4FBox.**  $^{18}\text{F}$  was obtained via the  $^{18}\text{O}$  (p,n)  $^{18}\text{F}$  reaction (IBA cyclotron 18/9 cyclotron). Fluoro substitution of the precursor was performed on a standard Neptis synthesizer (ORA). After the initial fluoride preparation (collection, drying, and Kryptofix activation), 1.0–2.0 mg of the radiolabeling precursor of [ $^{18}\text{F}$ ]BF227, [ $^{18}\text{F}$ ]2FBox, or [ $^{18}\text{F}$ ]4FBox was introduced, and the reaction mixture was heated at 150 °C for 10 min in DMSO (Figure 2). The reaction mixture was passed through an activated C18 cartridge for pre-purification, and the crude product was eluted from the cartridge with methanol. Pure [ $^{18}\text{F}$ ]BF227 was obtained after separation on a preparative high-performance liquid chromatography HPLC. For biological use, the product was diluted with sterile water, loaded onto a C18 cartridge (SEP-Pak Light, Waters), eluted with ethanol, and diluted with isotonic saline to an ethanol concentration of 5%. Quality control of [ $^{18}\text{F}$ ]BF227, [ $^{18}\text{F}$ ]2FBox, or [ $^{18}\text{F}$ ]4FBox consisted in determining the radiochemical purity and specific activity by analytic HPLC assay (UV and radioactive detections). The identity of [ $^{18}\text{F}$ ]BF227, [ $^{18}\text{F}$ ]2FBox, or [ $^{18}\text{F}$ ]4FBox was confirmed by co-injection with an authentic nonradioactive sample.

**Screening Material. Preparation of Fibrils.** Lyophilized  $\alpha$ -syn protein and amyloid- $\beta$  1–42 (A $\beta$ 42) peptide (recombinant human proteins, rPeptide) were dissolved in water for injection (WFI) with 0.02% azide to a final concentration of 200  $\mu\text{M}$ . The solutions were incubated at 37 °C with constant agitation at 250 rpm using a thermomixer (Thermo-Shaker PHnT, Grant-bio). Fibril aggregation was confirmed through thioflavin S (ThS) fluorescence staining.

**Injected Rats.** In order to evaluate both the ability of radiotracer candidates to cross the BBB and to detect  $\alpha$ -syn and A $\beta$ 42 fibrils, a model of rat was designed. These animals constitute robust, easy to implement and control animal models of proteinopathies. Adult male Sprague–Dawley rats

(8–9 weeks old) weighing 250–400 g were used (Charles River Laboratories, L'Arbresle, France). All animal experiments were performed in accordance with the European guidelines (2010/63/UE) and were approved by the Animal Use Ethics Committee of the University of Lyon (C2EA-42; Comité d'Ethique en Expérimentation Animale Neurosciences Lyon; celyne.lyon@inserm.fr). Rats were anesthetized with isoflurane inhalation in air (4% isoflurane in 1 L/min air) and then transferred to a stereotaxic apparatus (Stoelting, USA) equipped with a mask delivering isoflurane at 1.25–2.5% for the duration of the experiment. Body temperature was maintained by a heating pad set at 37 °C and monitored rectally. A pulse oximeter was used to measure the heart rate, respiratory rate, and oxygen saturation. Pain was controlled by the potent opioid analgesic buprenorphine (Buprecare, Axience) injected subcutaneously at a dose of 0.05 mg/kg 20 min before any surgical act was performed. Animals ( $n = 7$ ) were stereotaxically injected (1 nmol in 5  $\mu\text{L}$  per injection site) with pre-aggregated A $\beta$ 42 at the level of the caudate putamen (CPU) and  $\alpha$ -syn in the contralateral CPU, randomly (stereotaxic coordinates relative to bregma: AP = -3.2 mm; ML =  $\pm$  1.2 mm; DV = -3.6 mm), according to the stereotaxic atlas of the rat brain.<sup>21</sup> Fibrils were slowly infused at a constant rate of 1  $\mu\text{L}/\text{min}$  with 30-gauge needles. The needles were left in place for 2 min and then slowly withdrawn. After injections, the scalp was sutured, an antiseptic (povidone-iodine) and local analgesic (lidocaine) were applied, and the rats were allowed to recover from anesthesia. A 7-day post-injection interval was observed before euthanasia and subsequent studies.

**Transgenic Mice.** The “accelerated” version of the transgenic (Tg) mouse model (M83) expressing human A53T mutated  $\alpha$ -syn was obtained.<sup>22</sup> In this accelerated model,  $\alpha$ -syn aggregates appear  $\sim$ 100 days after inoculation, especially in the brainstem and midbrain.<sup>22</sup> This period corresponded to the age of the animal used for *in vitro* autoradiography brain sections. C57Bl/6S brain sections of a mouse presenting a deletion of the  $\alpha$ -syn locus ( $\alpha$ -syn KO) (Harlan, Gannat, France) were used as control. The transgenic mouse model (PDAPP line J20), overexpressing 2 human mutations of APP genes,<sup>23</sup> was obtained from collaborators (Dr. N. Rama, CRCL, UMR INSERM 1052, CNRS 5286, Lyon). Animal brain sections were used when they expressed large A $\beta$  plaques in the hippocampus and cortex.

**Human Postmortem Brains.** Human brain tissue sections were obtained as frozen sections from London Neurodegenerative Diseases Brain Bank and a local brain bank in Lyon (Cardiobiotec, HCL). Consecutive medulla sections from patients with various synucleinopathies were used for *in vitro* autoradiography. These included one PD patient (79 year-old male), one MSA patient (71 year-old male), and one control patient (63 year-old female). Consecutive brain sections, at the level of the cortex and hippocampus, from one AD patient (67 year-old male) were also included in the *in vitro* autoradiography experiments.

**In Vitro Binding Assay.** Synthetic  $\alpha$ -syn and A $\beta$ 42 fibrils (200 nM) were incubated with increasing concentrations of radiotracer (0.5–200 nM). In order to evaluate the nonspecific binding of the compounds, the below-mentioned reactions were performed in the presence of a 50  $\mu\text{M}$  unlabeled compound. Samples were incubated for 1 h at room temperature in 200  $\mu\text{L}$  of assay buffer (phosphate buffer saline: PBS, 0.1% bovine albumin serum: BSA). Bound

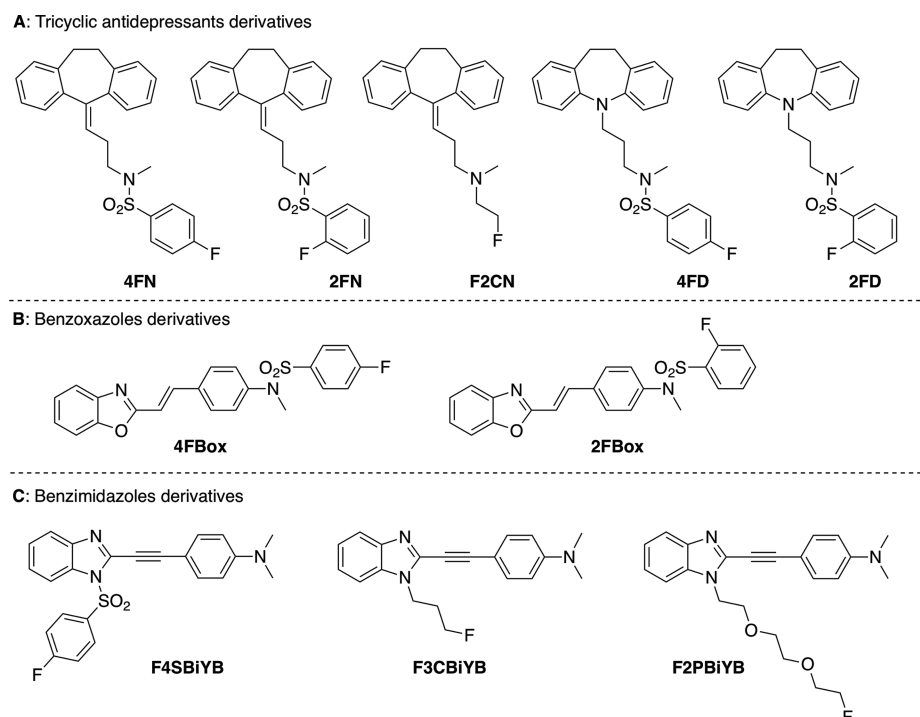


**Figure 3.** Diagram of the 10 molecules derived from three structural families with (A) the antidepressant tricyclic derivatives, (B) the benzoxazoles derivatives, and (C) the benzimidazoles derivatives.

radiolabeled tracer was separated from the free tracer by filtration under reduced pressure (Multiscreen HTS Vacuum Manifold; Multiscreen HTS-FB 1.0/0.65  $\mu\text{m}$ , Millipore). Filters were washed three times with 200  $\mu\text{L}$  of PBS. Washed filters were assayed for radioactivity by a gamma counter (Gamma Wizard 2480–160715, PerkinElmer). Binding data were analyzed with curve-fitting software that calculated  $K_d$  and  $B_{\text{max}}$  on a nonlinear regression (GraphPad Software, Prism 5). All experiments were conducted in triplicate.

**In Vivo Small-Animal PET Imaging.** Fibril-injected ( $n = 5$ ) and noninjected control rats ( $n = 5$ ) were used for *in vivo* PET imaging experiments in isoflurane-anesthetized animals (4% induction and 2% maintenance). Each experiment was performed in duplicate for each group (fibril-injected vs noninjected) and for each radiotracer ( $[^{18}\text{F}]\text{BF227}$ ,  $[^{18}\text{F}]\text{2FBox}$ , and  $[^{18}\text{F}]\text{4FBox}$ ). PET scans were acquired in the list mode, using a Siemens INVEON PET/CT scanner, with a nominal in-plane resolution of  $\sim 1.4$  mm full-width-at-half-maximum in the center of the FOV. A 60 min list mode acquisition started immediately after the caudal intravenous injection of  $[^{18}\text{F}]\text{BF227}$ ,  $[^{18}\text{F}]\text{2FBox}$ , or  $[^{18}\text{F}]\text{4FBox}$ . The reconstructed images led to a volume of 159 slices of  $128 \times 128$  voxels, with a voxel size of  $0.388 \times 0.388 \times 0.796$  mm. The dynamic images obtained were analyzed on the INVEON Research Workplace (IRW, Siemens).

PET was coregistered with CT, and both were coregistered with our in-house rat MRI atlas,<sup>24</sup> to extract radioactivity values in the whole brain (general brain uptake) but also in the region of interest (ROI), the CPU, where the fibrils were injected. Time activity curves (TAC) were expressed as the percentage of injected dose per gram (%ID/g) and standardized uptake values (SUV)<sup>25</sup> over time. SUV summed over the 40–60 min period (where TAC plateaued) were also calculated at the fibril-injected sites (CPU) and divided by the SUV measured in an area devoid of fibrils (cerebellum (Cb))

to give an index of radiotracer uptake (SUV ratio =  $\text{SUV}_{\text{CPU}} / \text{SUV}_{\text{Cb}}$ ).

**In Vitro Autoradiography.** Animals (fibril-injected rats and transgenic mice) were deeply anesthetized with isoflurane in the inducing chamber (4% isoflurane in 1 L/min air flow) and rapidly euthanized by decapitation. Brains were dissected and frozen in 2-methylbutane with dry ice ( $-30$  °C). Thirty-micrometer sections were cut across the respective ROIs: coronal CPU sections for fibril-injected rats, sagittal sections encompassing midbrain and brainstem for M83 mice, and sagittal sections through the hippocampus and cortex for PDAPP transgenic mice. Sections were then thaw-mounted on slides (Superfrost, Roth, France) and allowed to air-dry for 30 min before storage at  $-80$  °C until use. On the day of tracer synthesis, the slides (animal and human postmortem) were allowed to thaw at RT for 30–60 min, and sections were incubated at room temperature (RT) for 30 min in Tris-buffered saline (TBS) supplemented with HCl (TBS-HCl buffer) (138 mM NaCl, 2.7 mM KCl, pH adjusted to 7.5) containing 37 kBq/mL of either  $[^{18}\text{F}]\text{BF227}$ ,  $[^{18}\text{F}]\text{2FBox}$ , or  $[^{18}\text{F}]\text{4FBox}$ . After incubation, slides were dipped twice in an 8:1 ethanol/water mixture at RT for 1 min, then dried under cool air, and exposed on a sensitive phosphor imaging plate (BAS-IP MS 2025, Fujifilm) overnight. The distribution of radioactivity was then qualitatively visualized on a Bioimaging analyzer system (BAS-5000, Fujifilm).

**Immunofluorescence.** The frozen sections used for *in vitro* autoradiography or adjacent frozen brain sections were used for immunofluorescence studies. Brain sections were postfixed in 4% paraformaldehyde in PBS for 20 min, followed by 3 PBS washes of 5 min each, and transferred to a PBS solution (0.02% azide) at 4 °C until use. An antigen retrieval/unmasking step was conducted with 99% formic acid solution for 10 min followed by 3 PBS washes of 5 min each. Slides were then dipped in blocking and permeabilization buffer

(PBST with 5% BSA and 0.5% Triton X-100) for 30 min followed by 3 PBS washes of 5 min each. Incubation in PBST containing primary antibodies was then performed overnight at 4 °C. The primary antibodies used were the 4G8 clone for A $\beta$  (1/1000; anti- $\beta$ -amyloid, 17–24 antibody, mouse IgG2b) or the 5G4 clone for  $\alpha$ -syn (1/1000; anti-aggregated  $\alpha$ -synuclein, monoclonal mouse IgG1 $\kappa$ , kindly provided by Dr Ingolf Lachmann). Slides were then incubated in PBST containing the secondary antibody Alexa Fluor 594 (1/1000; AF594 anti-mouse, LifeTechnologies) for 1 h at room temperature followed by 3 PBS washes of 5 min each. Alternatively to immunofluorescence, ThS staining was performed with 0.0025%.

Fluorescence was first observed using an imaging microscope (Axioplan-2, Zeiss; Oberkochen, Germany). A Texas Red (ex 587  $\pm$  25 nm, em 647  $\pm$  70 nm) filter was used for the AF594 secondary antibody and a GFP (ex 470  $\pm$  40 nm, em 525  $\pm$  50 nm) filter for ThS. Images were captured using a digital camera interfaced with image-analysis software (Axiovision 3.0 software, Zeiss). Fluorescence was then observed and captured with a digital slide scanner (Axio Scan.Z1, Zeiss) (CIQLE Imaging Platform, University of Lyon, France) equipped with similar filters, in order to have a full view and digital image of each brain section. For human postmortem immunofluorescence images, the green channel (nonspecific autofluorescence binding) was subtracted (Adobe Photoshop CS6 tool) from the red channel in order to obtain images with only red specific immunolabeling.

## RESULTS

**Chemical Design.** The chemical design of ten candidate molecules derived from three structural families that demonstrated moderate to high affinity toward  $\alpha$ -syn fibrils, and modified to be easily radiolabeled with  $^{18}\text{F}$ , were explored.

The first structural family consisted of tricyclic antidepressants that were mentioned in a patent that demonstrated an interesting binding of imipramine and nortryptiline toward  $\alpha$ -syn fibrils.<sup>15</sup> Five fluorinated compounds (4FN, 2FN, 4FD, 2FD, and F2CN) were drawn (Figure 3A).

Inspired by the structure of the dyes used in histochemistry to reveal the  $\alpha$ -syn aggregates in postmortem studies, and from whom BF227 was derived,<sup>11</sup> the second family consisted of benzoxazoles derivatives. The benzoxazole-vinyl cores were conserved with the aim to reproduce and improve these binding properties (Figure 1). The pharmaco-modulation focused on the amino-thiazole part which was substituted by an amino-benzene moiety. A benzenesulfonyl part was also added on the amino function to allow a subsequent facilitated radiolabeling with  $^{18}\text{F}$ . These structures have a poly-conjugated planar structure interesting for interactions with  $\beta$ -sheet structures of  $\alpha$ -syn fibrils. Two candidate molecules were developed: 2FBox and 4FBox (Figure 3B).

The last series of molecules were derived from benzimidazoles derivatives which demonstrated moderate  $\alpha$ -syn binding affinity but 2–3 fold higher selectivity toward  $\alpha$ -syn in comparison to amyloid- $\beta$  aggregates.<sup>16–18</sup> For some of these compounds having demonstrated an *E/Z* double-bond isomerization,<sup>13</sup> the central double bonds were replaced by a triple bond to conserve the conjugation of the structure without isomerization abilities. With their planar structure, these benzimidazoles derivatives present promising conformation in order to bind (through  $\pi$ - $\pi$  interactions) to the channels formed along the  $\beta$ -sheet fibrils/filaments. Three candidate

molecules were developed and included F4SBiYB, F3CBiYB, and F2PBiYB (Figure 3C).

**Computational Modeling, Docking Site Identification, and Accessibility.** *Modelization of the  $\alpha$ -syn Fibrils.* The sequence of  $\alpha$ -syn was obtained from the UniProt database ([www.uniprot.org](http://www.uniprot.org)) under the reference P37840-1. Modeling of  $\alpha$ -syn fibril structure was based on a cryo-electron microscopy (cryo-EM) study<sup>20</sup> and consisted in a fragment of  $\alpha$ -syn fibrils with two entwined, asymmetrically associated protofibrils. A portion of the  $\alpha$ -syn fibril with 36  $\alpha$ -syn proteins (18 layers of duplicated  $\alpha$ -syn proteins) was reproduced in an all-atoms resolution. After a molecular dynamic of 20 ns in the isothermal–isobaric ensemble, 5 representative conformations of the fibril were sampled by 2D-RMSD (root-mean-square deviation), in which a common interaction site was identified by Site Finder. This site was oriented parallel to the fibril axis, located between amino-acids 67 and 75 of the  $\alpha$ -syn protein, and formed a loop in the fibril (Figure S.1A).

**Docking Scores.** Computation of docking simulations gave a score evaluating the affinity of all of our 10 candidate molecules for the identified docking site (with the highest pseudo-affinities for the lowest numerical values). The tricyclic antidepressant family was the one that showed, overall, the least interesting docking scores (Table 1). The benzimidazoles

**Table 1. Docking Scores of Our Candidate Molecules toward the Identified Docking Site on the  $\alpha$ -Syn Fibril Model<sup>a</sup>**

structural families	candidate molecules	$\alpha$ -syn fibril docking scores (kcal/mol)
tricyclics	4FD	−4.3
	2FN	−3.9
	4FN	−3.5
	2FD	−3.4
	F2CN	−3.2
benzoxazoles	4FBox	−9.0
	2FBox	−8.7
additional info	BF227	−8.3
benzimidazoles	F3CBiYB	−6.5
	F2PBiYB	−6.4
	F4SBiYB	−5.0

<sup>a</sup>Values are expressed in kcal/mol and reflect pseudo-affinities (the highest pseudo-affinities for the lowest values). Scores presented are GBVI/WAS (generalized-born volume integral/weighted surface area).

derivatives' docking scores varied from −5.0 to −6.5 kcal/mol. The benzoxazoles derivatives were the ones with the highest docking scores toward the identified  $\alpha$ -syn binding pocket with an improved docking score in comparison to BF227 (docking score for 4FBox = −9.0 kcal/mol, 2FBox = −8.7 kcal/mol, and BF227 = −8.3 kcal/mol). The docking results showed that the chemical modifications brought to BF227 derivatives' 2FBox and 4FBox were not predicted to annihilate their binding to the  $\alpha$ -syn fibril.

**Ability To Reach the Docking Site.** Umbrella sampling calculations (highly demanding in terms of computing power) were only performed for the two candidate molecules that demonstrated the highest docking scores toward the  $\alpha$ -syn binding pocket, namely, 2FBox and 4FBox. The identified radiotracer interaction site was deeply buried within the  $\alpha$ -syn structure. Candidate molecules must thus penetrate the

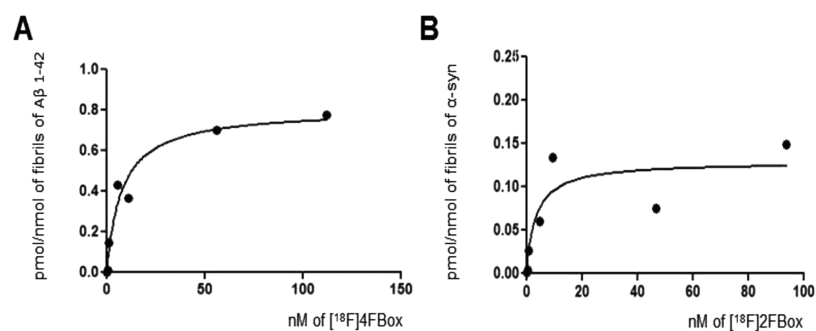


**Figure 4.** *In vitro* binding assays. (A) Saturation binding curve for [ $^{18}\text{F}$ ]4FBox specific binding to  $A\beta_{42}$  fibrils. (B) Saturation binding curve for [ $^{18}\text{F}$ ]2FBox specific binding to  $\alpha$ -syn fibrils.

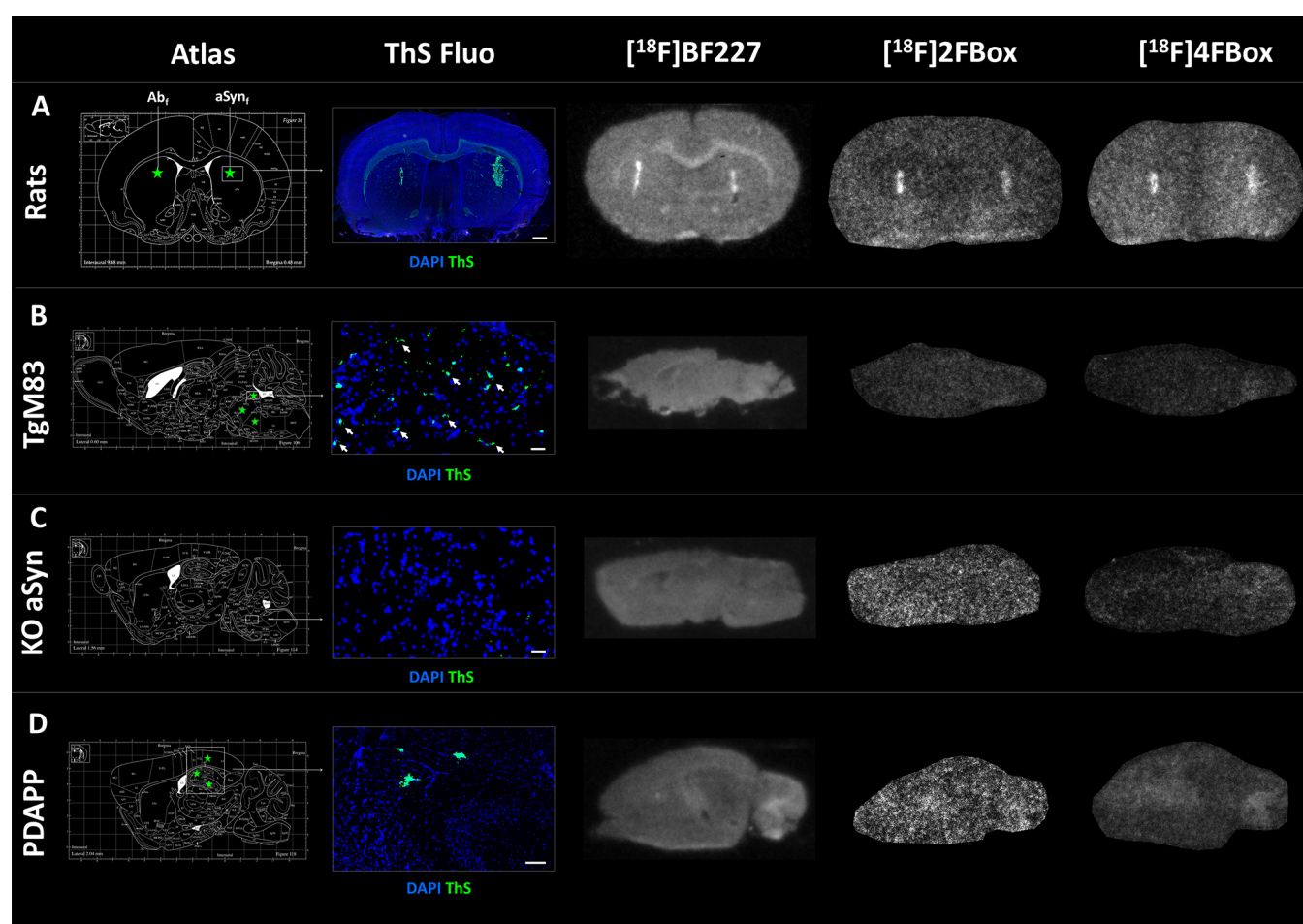


**Figure 5.** *In vitro* autoradiography with [ $^{18}\text{F}$ ]BF227, [ $^{18}\text{F}$ ]2FBox, and [ $^{18}\text{F}$ ]4FBox in animal models. (A) Fibril-injected rats; (B) M83 transgenic mice expressing human mutated form of  $\alpha$ -syn; (C)  $\alpha$ -syn knockout transgenic mouse model; and (D) PDAPP transgenic mouse model overexpressing 2 mutated forms of the human amyloid precursor protein. On the left, stereotaxic atlas figures of the anatomical level represented in the various animal models (green stars indicate fibril-injection sites). Green ThS fluorescence images illustrate the localization (white arrows) and confirm the presence of  $\alpha$ -syn and  $A\beta$  aggregates in the various animal models (DAPI blue fluorescence indicates cell nuclei). Scale bars represent 200  $\mu\text{m}$  in rats and PDAPP mice, and 20  $\mu\text{m}$  in M83 and  $\alpha$ -syn KO mice.

structure between the strand ladders to reach the interaction site. In order to simulate and calculate an energy profile for the whole access process, umbrella sampling simulations were performed. Calculation speed was enhanced by extracting a fragment of 13  $\alpha$ -syn proteins in which the sequence was reduced to amino acids 35–91. The potential of mean force results (PMF) graphical illustration is the umbrella sampling method we chose to reflect the accessibility of our candidate molecules to the interaction site (Figure S.1B). The energetic

barrier was the highest for 2FBox (7.1 kcal/mol), intermediate for 4FBox (6.5 kcal/mol), and the lowest for BF227 (6 kcal/mol). PMF for 4FBox and 2FBox showed similar profiles and penetration patterns.

**Candidate Molecules and Radiolabeling.** *Synthesis of Nonradioactive FBox Compounds and Their Precursors for Radiolabeling.* The nonradioactive FBox compounds and their precursors for radiolabeling (NBox) were synthesized following a divergent strategy (Figure 1). The common intermediate

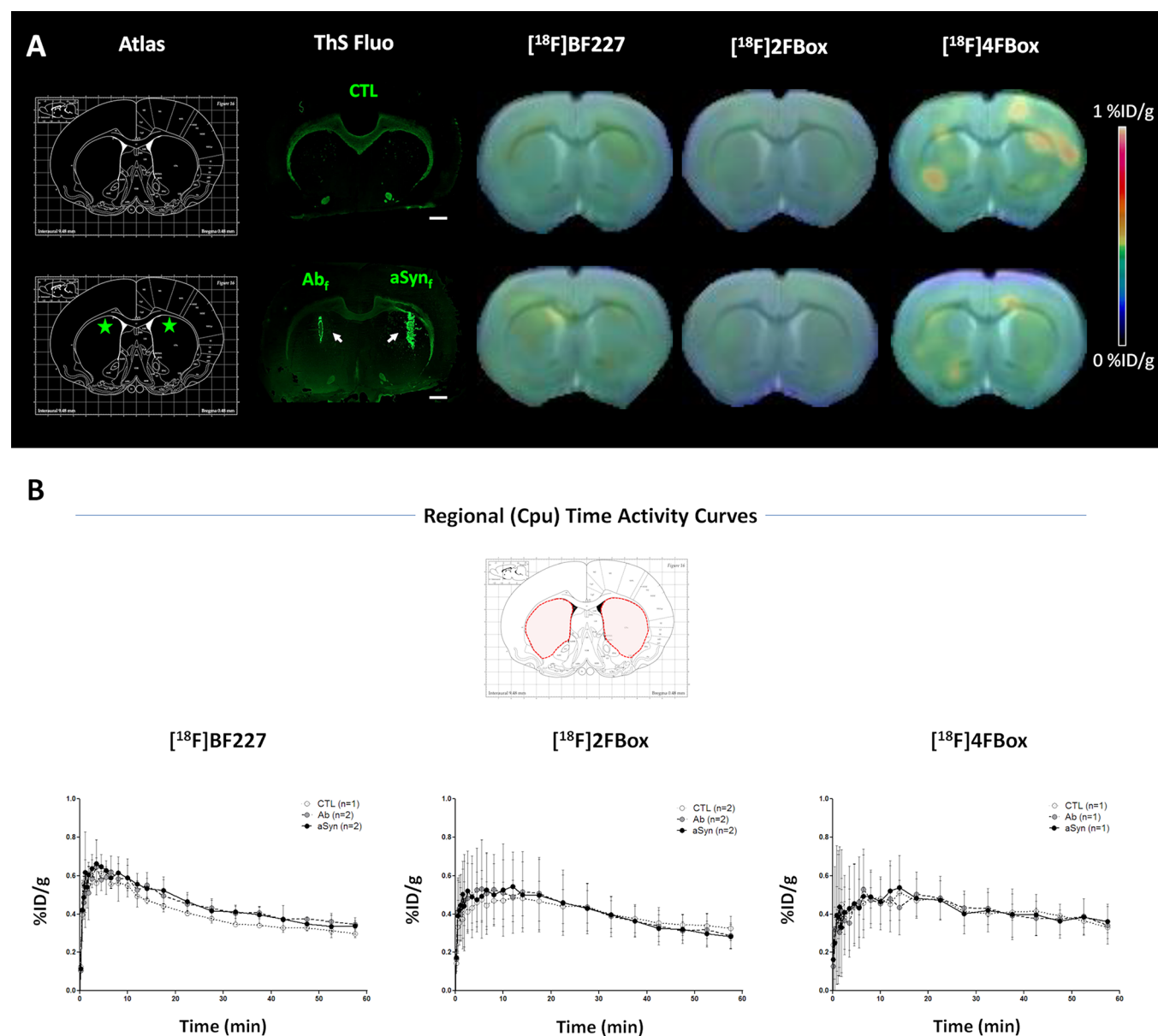


**Figure 6.** Small-animal PET imaging with  $[^{18}\text{F}]\text{BF227}$ ,  $[^{18}\text{F}]\text{2FBox}$ , and  $[^{18}\text{F}]\text{4FBox}$  in control and fibril-injected rats. (A) Summed PET images were coregistered with CT images, and the radioactivity index was reflected by a color scale representing %ID/g. ThS fluorescence staining of A $\beta$ 42 and  $\alpha$ -syn fibrils injected in the striata is presented (white arrows), with the corresponding stereotaxic brain atlas region (green stars representing injection sites). Scale bar represent 1 mm on ThS fluorescence staining. (B) Time activity curves (expressed in %ID/g over time) for each radiotracer are presented. Values (mean  $\pm$  SD) were extracted from the striata regions thanks to an in-house made MRI atlas that was coregistered to PET-CT images.

4 was obtained from the reaction between 2-methylbenzoxazole (1) and aldehyde 2, followed by Boc deprotection of the obtained compound 3. The FBox molecules could be then obtained through reaction with the corresponding fluorobenzenesulfonyl chloride (ortho-substituted for  $N$ -{4-[( $E$ )-2-(1,3-benzoxazol-2-yl)ethenyl]phenyl}-2- $[^{18}\text{F}]\text{fluoro-}N$ -methylbenzenesulfonamide (2FBox) and para-substituted for  $N$ -{4-[( $E$ )-2-(1,3-benzoxazol-2-yl)ethenyl]phenyl}-4- $[^{18}\text{F}]\text{fluoro-}N$ -methylbenzenesulfonamide (4FBox)). Similarly, NBox compounds were formed from the corresponding nitrobenzenesulfonyl chloride (ortho-substituted for  $N$ -{4-[( $E$ )-2-(1,3-benzoxazol-2-yl)ethenyl]phenyl}- $N$ -methyl-2-nitrobenzenesulfonamide (2NBox) and para-substituted for  $N$ -{4-[( $E$ )-2-(1,3-benzoxazol-2-yl)ethenyl]phenyl}- $N$ -methyl-4-nitrobenzenesulfona-

mid (4NBox)). The overall yields of these 3-step syntheses were generally satisfactory to good.

The radiolabeled compounds were obtained successfully through nucleophilic substitution of nitro group from 4NBox and 2NBox, with satisfactory radiochemical yields (10–19%) (Figure 2). Specific activity (SA) was relatively high (range, 68–543 GBq $\mu\text{mol}^{-1}$ ) for our 2 tracers. The log $D$  values were in accordance with good permeation of the BBB (Figure 2).

*In Vitro Radioactive Saturation Assays.*  $[^{18}\text{F}]\text{BF227}$ ,  $[^{18}\text{F}]\text{4FBox}$ , and  $[^{18}\text{F}]\text{2FBox}$  selectivity were tested against synthetic  $\alpha$ -syn and A $\beta$ 42 fibrils. First, successful formation of fibrils from recombinant proteins<sup>26</sup> was determined by ThS staining and direct observation of fibrils from recombinant proteins by transmission electronic microscopy (Figure S.2). According to the literature,<sup>11</sup> for  $[^{18}\text{F}]\text{BF227}$ ,  $K_d$  was equal to

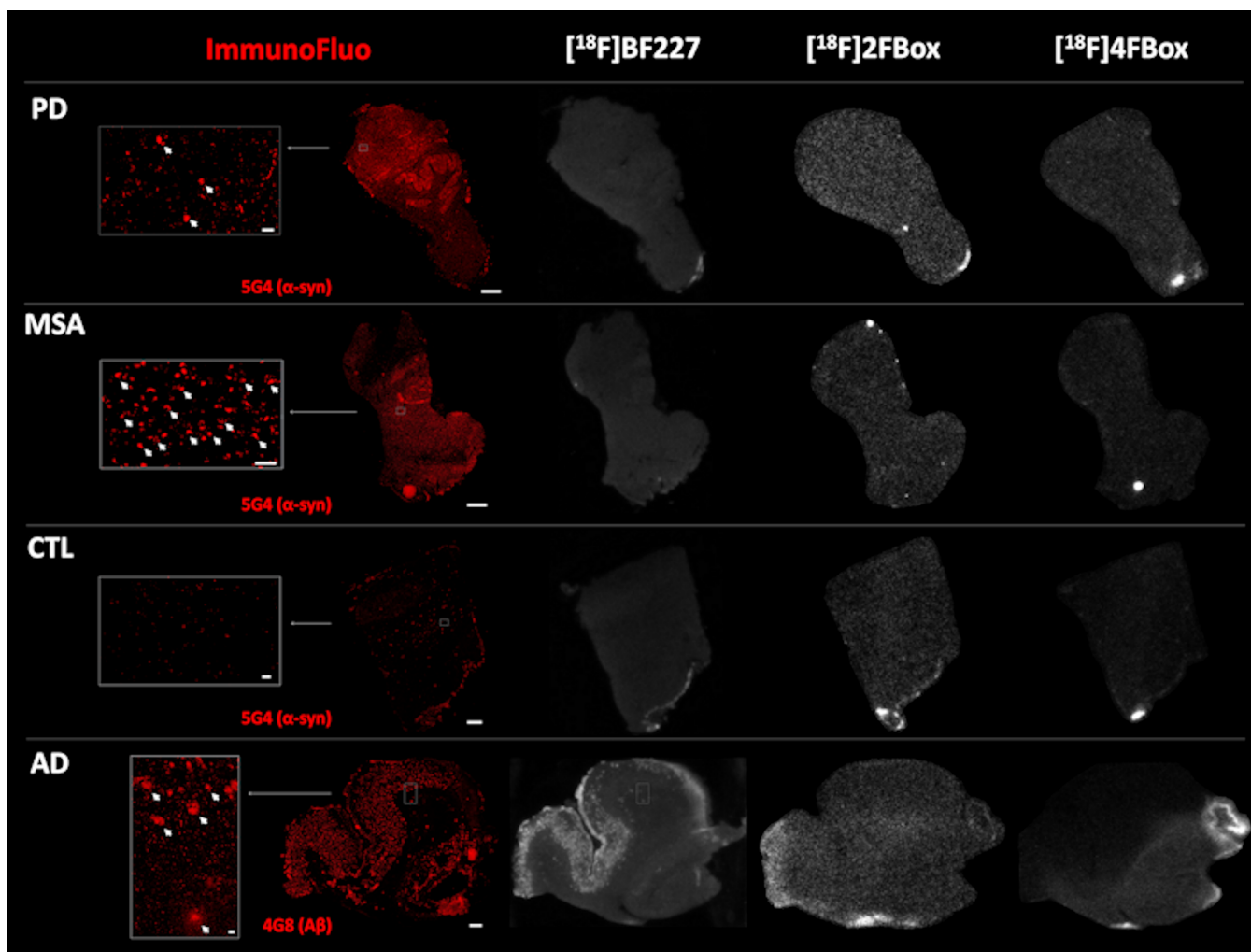


**Figure 7.** *In vitro* autoradiography with [ $^{18}\text{F}$ ]BF227, [ $^{18}\text{F}$ ]2FBox, and [ $^{18}\text{F}$ ]4FBox in *postmortem* human brain. (A) PD patient, (B) MSA patient, and (C) control patient medulla oblongata, and (D) AD patient cortex and hippocampus region. Left: immunofluorescence staining with  $\alpha$ -syn proteins labeled with the 5G4 antibody and  $A\beta$  proteins with the 4G8 antibody (white arrows). Scale bars in the zoom box represent 50  $\mu\text{m}$  in PD, MSA, and CTL, and 100  $\mu\text{m}$  in AD brain. In the digitized whole-brain sections, scale bars represent 2 mm. Note that only [ $^{18}\text{F}$ ]BF227 was able to label  $A\beta$  plaques in the AD patient, as demonstrated by the co-localization of the [ $^{18}\text{F}$ ]BF227 radioactive signal (in white) and 4G8 immunostaining (in red).

$14.03 \pm 43.52$  nM and  $B_{\text{max}} = 11.98 \pm 9.49$  pmol/nmol of fibrils for  $\alpha$ -syn fibrils. For  $A\beta_{42}$  fibrils,  $K_{\text{d}1}$  was equal to  $0.82 \pm 1.08$  nM and  $B_{\text{max}1} = 0.91 \pm 0.41$  pmol/nmol of fibrils, while  $K_{\text{d}2}$  was equal to  $125.2 \pm 29.05$  nM to  $A\beta_{1-42}$  and  $B_{\text{max}2} = 14.43 \pm 10.07$  pmol/nmol of fibrils (Figure S.3). [ $^{18}\text{F}$ ]4FBox bound with low affinity to  $\alpha$ -syn fibrils ( $K_{\text{d}} = 155.4 \pm 96.5$  nM and  $B_{\text{max}} = 2.073 \pm 0.821$  pmol/nmol of fibrils) and with better affinity to  $A\beta_{42}$  fibrils ( $K_{\text{d}} = 7.7 \pm 2.6$  nM and  $B_{\text{max}} = 0.802 \pm 0.070$  pmol/nmol of fibrils, Figure 4). In contrast, [ $^{18}\text{F}$ ]2FBox bound  $\alpha$ -syn fibrils with a high affinity ( $K_{\text{d}} = 3.3 \pm 2.8$  nM and  $B_{\text{max}} = 0.128 \pm 0.025$  pmol/nmol of fibrils) and with a lower affinity to  $A\beta_{42}$  fibrils ( $K_{\text{d}} = 145.3 \pm 114.5$  nM and  $B_{\text{max}} = 0.592 \pm 0.251$  pmol/nmol of fibrils).

***In Vitro* Autoradiography in Rats and Mice.** In the striata of fibril-injected rats, all three radiotracers were able to nonselectively detect  $\alpha$ -syn and  $A\beta_{42}$  synthetic fibrils in autoradiography experiments, as shown by the intense radioactive signal located on the site where immunofluorescence confirmed the presence of aggregated  $\alpha$ -syn and  $A\beta_{42}$  fibrils (Figure 5).

In the midbrain and brainstem of the Tg mouse model overexpressing a mutated form of  $\alpha$ -syn (M83) and in the cortex and hippocampus of the Tg mouse model overexpressing 2 mutated forms of APP (PDAPP line 20), none of the three radiotracers were able to detect the  $\alpha$ -syn or  $A\beta$  aggregates stained with ThS (Figure 5). The Tg mouse model lacking  $\alpha$ -syn expression, as confirmed by absence of ThS staining, gave a similar negative radioactive signal (Figure 5).

***In Vivo* PET Imaging in Rats.** The PET imaging study was performed in our rat model, which exhibited an  $\alpha$ -syn on one side and  $A\beta_{42}$  fibrils on the other side of the CPU, compared to the noninjected rat. The 60 min acquisition started immediately after caudal intravenous injection of [ $^{18}\text{F}$ ]BF227 ( $10.9 \pm 5.5$  MBq; range, 7.4–17.2 MBq), [ $^{18}\text{F}$ ]2FBox ( $12.4 \pm 1.8$  MBq; range, 10.8–14.9 MBq), or [ $^{18}\text{F}$ ]4FBox ( $9.4 \pm 6.6$  MBq; range, 4.7–14.1 MBq). Biological evaluation of the three radiotracers indicated crossing of the BBB and entry to the brain (Figure 6). Initial whole-brain uptake was higher and faster with [ $^{18}\text{F}$ ]BF227 (0.65%ID/g peak at 2 min post-injection (p.i.)) than with [ $^{18}\text{F}$ ]4FBox (0.47%ID/g peak at 10 min p.i.) or [ $^{18}\text{F}$ ]2FBox (0.47%ID/g peak at 12 min p.i.).

Standardized uptake values (SUV) approximating 2 at a peak are usually desirable for PET brain radiotracers.<sup>27</sup> Calculated SUV at a peak was close to 2, with values of 2.7, 1.6, and 1.6 for [<sup>18</sup>F]BF227, [<sup>18</sup>F]4FBox, and [<sup>18</sup>F]2FBox, respectively. The washout kinetics was moderate, with half of the overall brain activity (calculations performed on the whole brain activity) still present after 60 min (5 min/60 min ratio: 2.2 for [<sup>18</sup>F]BF227, 1.7 for [<sup>18</sup>F]2FBox, and 1.5 for [<sup>18</sup>F]4FBox). Injected fibrils were not detected by any of the three radiotracers *in vivo* (Figure 6). Calculated SUVR (mean  $\pm$  SD) with [<sup>18</sup>F]BF227 was  $1.05 \pm 0.03$ ,  $1.10 \pm 0.12$ , and  $1.05 \pm 0.02$  in control, A $\beta$ 42, and  $\alpha$ -syn-injected striata, respectively. PET imaging with [<sup>18</sup>F]2FBox gave SUVR =  $1.08 \pm 0.02$ ,  $1.13 \pm 0.04$ , and  $1.10 \pm 0.02$  in control, A $\beta$ 42, and  $\alpha$ -syn-injected striata, respectively. Finally, [<sup>18</sup>F]4FBox did not perform better, with SUVR (mean  $\pm$  SD) of  $1.12 \pm 0.03$ ,  $1.05 \pm 0.06$ , and  $1.07 \pm 0.05$  in control, A $\beta$ 42, and  $\alpha$ -syn injected striata, respectively.

#### *In Vitro* Autoradiography in Postmortem Patients' Brain.

In human postmortem PD brain (medulla oblongata), none of the three radiotracers were able to image Lewy bodies or neurites, as seen from the absence of radioactive signal in these  $\alpha$ -syn rich regions immunostained by the 5G4 antibody, which preferentially labels aggregated synuclein<sup>28</sup> (Figure 7). In human postmortem MSA brain, where glial cytoplasmic  $\alpha$ -syn inclusions were immunostained by 5G4, no radioactive signal could be detected with any of the three radiotracers (Figure 7). Similarly, in control human postmortem brain, no radioactive signal or immunostaining could be detected (Figure 7). In the human postmortem AD brain, large A $\beta$  plaques were immunostained by the 4G8 antibody in the cortex and hippocampus. The [<sup>18</sup>F]BF227 signal clearly co-localized with 4G8 staining, and binding was displaced with nonradioactive BF227 in excess (data not shown). However, neither [<sup>18</sup>F]2FBox nor [<sup>18</sup>F]4FBox were able to detect A $\beta$  plaques (Figure 7).

## DISCUSSION

The development of an  $\alpha$ -syn PET radiotracer is particularly challenging, as indicated by the fact that all published attempts were failures. This general observation incited us to propose a slightly different screening paradigm to evaluate our PET candidates. Starting from a "classical" chemical design of candidate molecules derived from three structural families that demonstrated interesting  $\alpha$ -syn binding characteristics, we then developed a bioinformatics modelization approach (modelization of  $\alpha$ -syn fibrils, identification of docking site, and evaluation of candidate molecules docking scores and ability to reach the binding pocket) to select the "best" candidates and confirm the chemical choice before embarking in synthesis and radiolabeling, *in vitro* assays performed with synthetic fibrils, *in vitro/in vivo* imaging studies with animal models, and, finally, *in vitro* postmortem autoradiography studies.

From the design of 10 candidate molecules derived from three structural families, our objective was that this pharmacomodulation could bring interesting selectivity and specificity properties toward  $\alpha$ -syn fibrils. The cryo-EM  $\alpha$ -syn fibril model we used for subsequent computational modeling was relevant because fibrils are known to be composed of multiple protofibrils.<sup>29,30</sup> Even if a recent  $\alpha$ -syn fibril NMR structure has been characterized,<sup>31</sup> our model remained relevant as the NMR structure does not consider associations of multiple protofibrils. A recent study on A $\beta$  styrylbenzoxazole candidate

radiotracers showed that there was only a weak correlation between the docking scores and experimental binding affinities.<sup>32</sup> Therefore, our docking results only gave indications (no definitive answers) on which structural families were more interesting. The tricyclic antidepressants and benzimidazoles structural families were the least interesting, with low docking scores. However, the chemical modifications brought to BF227's structure to produce our benzoxazoles derivatives 2FBox and 4FBox did not result in a drop/fall in the docking scores. Overall, our computational modeling experiments suggested that these last two candidate molecules retained a binding ability similar to BF227 (docking scores), though at the price of a greater energy required to reach the binding site (umbrella sampling). We thus decided to attempt their radiolabeling with <sup>18</sup>F and succeeded.

Consecutive saturation filter binding assays with recombinant synthetic fibrils showed that [<sup>18</sup>F]2FBox was clearly the best of our two candidates. In our experimental conditions, [<sup>18</sup>F]2FBox detected  $\sim$ 16-fold less binding sites ( $B_{\max}$ ) on  $\alpha$ -syn fibrils than [<sup>18</sup>F]4FBox, but it did so with an  $\sim$ 47-fold better affinity ( $K_d$ ) and a nearly 44-fold selectivity toward  $\alpha$ -syn versus A $\beta$ 42 fibrils, when [<sup>18</sup>F]4FBox was more selective toward A $\beta$ 42 than  $\alpha$ -syn fibrils ( $\sim$ 20-fold). These results should nonetheless be interpreted with caution, as reproducibility issues were encountered. Though the filter binding assay is a robust technique for "receptology", it might be less well adapted to fibrils, a very different type of target, which consequently generated nonspecific, nonsaturable binding in our experiments. Indeed, cerebral aggregates and synthetic fibrils display a high propensity to coat to surfaces.<sup>33,34</sup> Another confounding feature of protein aggregates is their so-called structural polymorphism,<sup>35–37</sup> the formation of several types of fibril, distinguished by variable 3D structures (differences in folding in the formation of folded  $\beta$ -sheets) and variable quaternary structures. These conformational changes could lead to different binding sites on these fibrils for candidate radiotracers. An aggregation polymorphism was observed by electronic microscopy: a modification of pH or of aggregation time showed the formation of fibrils with different structures (data not shown). This heterogeneity of the structure may be the source of significant variability in the binding experiments, but it is also an opportunity for exploration with molecular imaging and computational modeling.

Evaluation in synthetic-fibril-injected rats demonstrated the ability of our radiotracers to nonselectively detect A $\beta$ 42 and  $\alpha$ -syn recombinant human fibrils *in vitro* and *ex vivo* (data are presented in Figure S.4). However, *in vivo* small-animal PET imaging in this same rat model showed that both radiotracers failed to detect either A $\beta$ 42 or  $\alpha$ -syn fibrils despite good uptake in cerebral tissue. This discrepancy between *in vivo* and *in vitro* results is probably due, in part, to the low spatial resolution of small-animal PET imaging<sup>38</sup> in comparison to *in vitro* autoradiography.<sup>39</sup> Low specific activity is another potential factor that has previously been implicated in the failure to detect A $\beta$  plaques in animal models of AD.<sup>40–42</sup> However, in the present study, specific activity was unlikely to be responsible for nondetection *in vivo*, as SA was relatively high (range, 68–543 GBq  $\mu$ mol<sup>-1</sup>) for both tracers.

Similarly, [<sup>18</sup>F]2FBox and [<sup>18</sup>F]4FBox were unable to detect A $\beta$  or  $\alpha$ -syn in the transgenic mouse models of Alzheimer's (PDAPP) and Parkinson's (M83) disease. [<sup>18</sup>F]BF227, a derivative of a well-known <sup>11</sup>C A $\beta$  radiotracer,<sup>43,44</sup> was not able

to image either  $\alpha$ -syn, as previously demonstrated by our team<sup>45</sup> or, more surprisingly,  $A\beta$  plaques. Hypotheses for this lack of  $A\beta$  plaques binding include methodological issues. It is known in PET imaging that radiotracer binding with good imaging contrast is a function of target-site density ( $B_{\max}$ ; higher is better) relative to radiotracer affinity to the binding site ( $K_d$ ; lower is better).<sup>46</sup> It may be that the density of  $\alpha$ -syn and  $A\beta$  plaque inclusions in these models were too low to achieve a good PET imaging contrast.<sup>45</sup> Concerning our candidate  $\alpha$ -syn radiotracers, in the “PD-like” accelerated Tg mouse model (M83) expressing the human A53T mutated  $\alpha$ -syn,<sup>22</sup> neither [<sup>18</sup>F]2FBox nor [<sup>18</sup>F]4FBox were able to detect  $\alpha$ -syn aggregates. Similarly, in the Tg mouse model (PDAPP line J20) overexpressing 2 human mutations of APP genes,<sup>23</sup> [<sup>18</sup>F]2FBox and [<sup>18</sup>F]4FBox were not able to image the confirmed presence of  $A\beta$  plaques. These negative results obtained with the Tg mouse models that overexpress human forms of the fibrils highlight the first “gap” between the feasibility of imaging synthetic recombinant human fibrils and the complexity of access to a binding site on human mutated fibrils produced in an animal model. In the search for an  $\alpha$ -syn PET radiotracer, a very important and difficult point is to find one or several animal models that accurately reflect human pathology.<sup>10</sup> Negative results in the search for an  $\alpha$ -syn PET imaging radiotracer highlight the challenges to overcome, particularly in terms of selectivity<sup>13</sup> and predictivity of the models.<sup>10</sup> The gold-standard will always be evaluation in human tissue and, ultimately, *in vivo* in patients.

Gold-standard *in vitro* autoradiography experiments in postmortem brain tissue of confirmed synucleinopathy cases, including PD and MSA, also failed to detect  $\alpha$ -syn aggregates in Lewy bodies or glial cytoplasmic inclusions, respectively. Several hypotheses can be put forward to explain these negative results. First, the size and density of the fibrils/aggregates:  $\alpha$ -syn aggregates are much smaller in size and lower in density than  $A\beta$  plaques. In AD patient brain,  $A\beta$  plaques were 60–200  $\mu\text{m}$  in diameter, while in PD brain, Lewy neurites were only 30–40  $\mu\text{m}$  ( $\sim 5$ -fold smaller).<sup>47,48</sup> Lewy neurites were even thinner (<10  $\mu\text{m}$  diameter) but rather long ( $\sim 600$   $\mu\text{m}$  long).<sup>49</sup> Glial cytoplasmic inclusions were 20–60  $\mu\text{m}$  in diameter.<sup>50</sup> Density was clearly low in PD brain, with only 6 Lewy bodies that could be observed in one section (while there were more glial cytoplasmic inclusions in MSA brain), whereas more than a hundred  $A\beta$  plaques could be counted in one section of AD brain. Additionally, not all  $A\beta$  plaques were actually detected by [<sup>18</sup>F]BF227. So there seem to be some  $A\beta$  plaques that do not have all characteristics necessary for [<sup>18</sup>F]BF227 to access its binding site. Alternatively, the  $A\beta$  plaques in one AD patient had different structures, enabling [<sup>18</sup>F]BF227 to bind only to certain  $A\beta$  plaques. The same argument could be applied to  $\alpha$ -syn radiotracers: that one good tracer is not able to bind to all  $\alpha$ -syn Lewy bodies, making the discovery of an  $\alpha$ -syn radiotracer even more challenging. It is, however, encouraging that some radiotracers do successfully target neuronal receptors present at even lower densities.<sup>6,13</sup> The negative results obtained with human postmortem brains highlight the second “gap” between the feasibility of imaging synthetic recombinant human fibrils and the complexity of accessing a binding site in human postmortem brain.

The discrepancy between results obtained with, on the one hand, computational modeling and recombinant human fibrils *in vitro* in injected rats and, on the other hand, *in vivo* with

postmortem human brain tissue casts doubt on the predictivity of computational modeling, on screening candidate molecules with recombinant human fibrils produced *in vitro*, and on evaluating candidate radiotracers with animal models that do not perfectly reflect the full pathology. To overcome this major issue, several strategies can be put forward. First, concerning computational modeling, the failure of the experimental studies compared to the *in silico* predictions may come from the use of an  $\alpha$ -syn fibril model that did not reflect the *in vivo* pathophysiology, as most information on  $\alpha$ -syn fibril structure comes only from fibrils produced *in vitro*. An interesting research axis would be to have access to fibril structures (NMR or cryo-EM) derived from patients. There may be an important gap between fibrillary polymorphisms obtained *in vitro* and those present in the brains of patients, because of both the maturation environment and the speed of aggregation. The second strategy would be to perform filter binding assays with human postmortem brain homogenates, as this is the reference method for quantification purposes.<sup>11,51–53</sup>

Another approach would be to produce fibrillary strains of  $A\beta$  and  $\alpha$ -syn by amplification of recombinant human peptides with patient material isolated from human samples in order to control structural polymorphism.

## ■ CONCLUSION

After the chemical design of 10 molecules derived from three structural families, bioinformatics modeling tools enabled us to select two original benzoxazole candidate ligands that were successfully labeled with <sup>18</sup>F. Evaluation in rats demonstrated the ability of both radiolabeled molecules to nonselectively detect  $A\beta$  and  $\alpha$ -syn recombinant human fibrils *in vitro*. However, small-animal PET imaging in this rat model showed that, although both candidate radioligands were able to cross the BBB, they failed to detect either  $A\beta$  or  $\alpha$ -syn fibrils *in vivo*. Similarly, [<sup>18</sup>F]2FBox and [<sup>18</sup>F]4FBox were unable to detect  $A\beta$  or  $\alpha$ -syn in the transgenic mouse models of Alzheimer's (PDAPP) and Parkinson's (M83) disease. Finally, gold-standard *in vitro* autoradiography experiments in postmortem brain tissue of confirmed synucleinopathy cases, including PD and MSA, also failed to detect  $\alpha$ -syn aggregates in Lewy bodies or glial cytoplasmic inclusions, respectively. [<sup>18</sup>F]2FBox and [<sup>18</sup>F]4FBox are not suitable  $\alpha$ -syn PET radiotracers. This study presented an experimental paradigm, theoretically adapted to the research of PET tracers for aggregated proteins, but it needs to be improved in terms of the predictivity of computational modeling in order to be ready for application in subsequent radiotracer candidates.

## ■ ASSOCIATED CONTENT

### 📄 Supporting Information

The Supporting Information is available free of charge on the ACS Publications website at DOI: 10.1021/acs.molpharmaceut.8b00229.

Localization of the interaction site on one of the two protofibrils constituted of 18  $\alpha$ -synucleins; PMF along the reaction coordinate (0.1A) for the 3 molecules, BF227, 4FBox, and 2FBox; TEM images of  $A\beta$ 42 fibrils and  $\alpha$ -syn fibrils; *in vitro* binding assays of [<sup>18</sup>F]BF227; saturation binding curve for [<sup>18</sup>F]BF227 specific binding to  $\alpha$ -syn fibrils; saturation binding curve for [<sup>18</sup>F]BF227 specific binding to  $A\beta$ 42 fibrils; and *ex vivo* auto-

radiography performed with [ $^{18}\text{F}$ ]BF227 and [ $^{18}\text{F}$ ]2FBox (PDF)

## AUTHOR INFORMATION

### Corresponding Author

\*E-mail: [elise.levigoureux@chu-lyon.fr](mailto:elise.levigoureux@chu-lyon.fr).

### ORCID

Elise Levigoureux: 0000-0003-1231-1036

Thierry Billard: 0000-0002-2937-9523

### Author Contributions

#M.V. and E.L. contributed equally to this work.

### Notes

The authors declare no competing financial interest.

## ACKNOWLEDGMENTS

Dr. Mathieu Verdurand was supported by a Young Researcher Grant from the Foundation Plan Alzheimer (Alzheimer Plan 2008-2017). This work was performed within the framework of the LABEX PRIMES (ANR-11-LABX-0063) of Lyon University, as part of the "Investissements d'Avenir" program (ANR-11-IDEX-0007) of the French National Research Agency (ANR). Dr. Thierry Baron of the French Agency for Food, Environmental, and Occupational Health & Safety (ANSES) is thanked for the generous gift of the transgenic M83 mouse model. Dr. Nicolas Rama is thanked for the generous gift of the transgenic PDAPP mouse model. Dr. Claire Troakes, of London Degenerative Brain Bank, is also thanked for her assistance in accessing human postmortem patient brain tissue. We thank all patients and their families for consent to use tissues in this research.

## ABBREVIATIONS

$\alpha$ -syn, alpha-synuclein;  $\tau$ , Tau protein; PET, positron emission tomography; PD, Parkinson disease; PDD, Parkinson disease with dementia; DLB, dementia with Lewy bodies; MSA, multiple system atrophy; BBB, blood brain barrier; 3D, three dimension; AD, Alzheimer's disease; TIP5P, 5-site transferable interaction potential; MOE, molecular operating environment; A $\beta$ 42, amyloid- $\beta$  1–42; WFI, water for injection; ThS, thioflavin S; CPU, Caudate putamen; Tg, transgenic; PBS, phosphate buffer saline; BSA, bovine serum albumin; IRW, INVEON Research Workplace; ROI, region of interest; TAC, time activity curves; SUV, standardized uptake values; SUVr, standardized uptake values ratio; PMF, potential of mean force; RT, room temperature; HPLC, High-Performance Liquid Chromatography

## REFERENCES

- (1) Golde, T. E.; Borchelt, D. R.; Giasson, B. I.; Lewis, J. Thinking laterally about neurodegenerative proteinopathies. *J. Clin. Invest.* **2013**, *123*, 1847–55.
- (2) Surguchov, A. Intracellular Dynamics of Synucleins: "Here, There and Everywhere". *Int. Rev. Cell Mol. Biol.* **2015**, *320*, 103–69.
- (3) Bauckneht, M.; Arnaldi, D.; Nobili, F.; Aarsland, D.; Morbelli, S. New tracers and new perspectives for molecular imaging in Lewy body diseases. *Curr. Med. Chem.* **2017**, *1*.
- (4) McKeith, I. G.; Boeve, B. F.; Dickson, D. W.; Halliday, G.; Taylor, J. P.; Weintraub, D.; Aarsland, D.; Galvin, J.; Attems, J.; Ballard, C. G.; Bayston, A.; Beach, T. G.; Blanc, F.; Bohnen, N.; Bonanni, L.; Bras, J.; Brundin, P.; Burn, D.; Chen-Plotkin, A.; Duda, J. E.; El-Agnaf, O.; Feldman, H.; Ferman, T. J.; Ffytche, D.; Fujishiro, H.; Galasko, D.; Goldman, J. G.; Gomperts, S. N.; Graff-Radford, N. R.; Honig, L. S.; Iranzo, A.; Kantarci, K.; Kaufer, D.; Kukull, W.; Lee,

V. M. Y.; Leverenz, J. B.; Lewis, S.; Lipka, C.; Lunde, A.; Masellis, M.; Masliah, E.; McLean, P.; Mollenhauer, B.; Montine, T. J.; Moreno, E.; Mori, E.; Murray, M.; O'Brien, J. T.; Orimo, S.; Postuma, R. B.; Ramaswamy, S.; Ross, O. A.; Salmon, D. P.; Singleton, A.; Taylor, A.; Thomas, A.; Tiraboschi, P.; Toledo, J. B.; Trojanowski, J. Q.; Tsuang, D.; Walker, Z.; Yamada, M.; Kosaka, K. Diagnosis and management of dementia with Lewy bodies: Fourth consensus report of the DLB Consortium. *Neurology* **2017**, *89*, 88–100.

(5) M J Fox Foundation, ALPHA-SYNUCLEIN IMAGING PRIZE. <https://www.michaeljfox.org/research/imaging-prize.html?navid=alpha-syn-image-prize> (2018).

(6) Eberling, J. L.; Dave, K. D.; Frasier, M. A. alpha-synuclein imaging: a critical need for Parkinson's disease research. *J. Parkinsons dis.* **2013**, *3*, 565–567.

(7) Kotzbauer, P. T.; Cairns, N. J.; Campbell, M. C.; Willis, A. W.; Racette, B. A.; Tabal, S. D.; Perlmutter, J. S. Pathologic accumulation of alpha-synuclein and Abeta in Parkinson disease patients with dementia. *Arch. Neurol.* **2012**, *69*, 1326–31.

(8) Trojanowski, J. Q. Emerging Alzheimer's disease therapies: focusing on the future. *Neurobiol. Aging* **2002**, *23*, 985–90.

(9) McKeith, I. G.; Dickson, D. W.; Lowe, J.; Emre, M.; O'Brien, J. T.; Feldman, H.; Cummings, J.; Duda, J. E.; Lipka, C.; Perry, E. K.; Aarsland, D.; Arai, H.; Ballard, C. G.; Boeve, B.; Burn, D. J.; Costa, D.; Del Ser, T.; Dubois, B.; Galasko, D.; Gauthier, S.; Goetz, C. G.; Gomez-Tortosa, E.; Halliday, G.; Hansen, L. A.; Hardy, J.; Iwatsubo, T.; Kalaria, R. N.; Kaufer, D.; Kenny, R. A.; Korczyn, A.; Kosaka, K.; Lee, V. M.; Lees, A.; Litvan, I.; Londos, E.; Lopez, O. L.; Minoshima, S.; Mizuno, Y.; Molina, J. A.; Mukaetova-Ladinska, E. B.; Pasquier, F.; Perry, R. H.; Schulz, J. B.; Trojanowski, J. Q.; Yamada, M. Diagnosis and management of dementia with Lewy bodies: third report of the DLB Consortium. *Neurology* **2005**, *65*, 1863–1872.

(10) Neal, K. L.; Shakerdige, N. B.; Hou, S. S.; Klunk, W. E.; Mathis, C. A.; Nesterov, E. E.; Swager, T. M.; McLean, P. J.; Bacskai, B. J. Development and screening of contrast agents for in vivo imaging of Parkinson's disease. *Molecular imaging and biology: MIB: the official publication of the Academy of Molecular Imaging* **2013**, *15*, 585–95.

(11) Fodero-Tavoletti, M. T.; Mulligan, R. S.; Okamura, N.; Furumoto, S.; Rowe, C. C.; Kudo, Y.; Masters, C. L.; Cappai, R.; Yanai, K.; Villemagne, V. L. In vitro characterisation of BF227 binding to alpha-synuclein/Lewy bodies. *Eur. J. Pharmacol.* **2009**, *617*, 54–8.

(12) Kikuchi, A.; Takeda, A.; Okamura, N.; Tashiro, M.; Hasegawa, T.; Furumoto, S.; Kobayashi, M.; Sugeno, N.; Baba, T.; Miki, Y.; Mori, F.; Wakabayashi, K.; Funaki, Y.; Iwata, R.; Takahashi, S.; Fukuda, H.; Arai, H.; Kudo, Y.; Yanai, K.; Itoyama, Y. In vivo visualization of alpha-synuclein deposition by carbon-11-labelled 2-[2-(2-dimethylaminothiazol-5-yl)ethyl]-6-[2-(fluoro)ethoxy]-benzoxazole positron emission tomography in multiple system atrophy. *Brain* **2010**, *133*, 1772–8.

(13) Bagchi, D. P.; Yu, L.; Perlmutter, J. S.; Xu, J.; Mach, R. H.; Tu, Z.; Kotzbauer, P. T. Binding of the radioligand SIL23 to alpha-synuclein fibrils in Parkinson disease brain tissue establishes feasibility and screening approaches for developing a Parkinson disease imaging agent. *PLoS One* **2013**, *8*, e55031.

(14) Chu, W.; Zhou, D.; Gaba, V.; Liu, J.; Li, S.; Peng, X.; Xu, J.; Dhavale, D.; Bagchi, D. P.; d'Avignon, A.; Shakerdige, N. B.; Bacskai, B. J.; Tu, Z.; Kotzbauer, P. T.; Mach, R. H. Design, Synthesis, and Characterization of 3-(Benzylidene)indolin-2-one Derivatives as Ligands for alpha-Synuclein Fibrils. *J. Med. Chem.* **2015**, *58*, 6002–17.

(15) Lansbury, P. T.; Justman, C. J.; Shinobu, L. Imaging of alpha-synuclein. Patent WO2009018088A2, 2009.

(16) Lee, J. H.; Lee, I. H.; Choe, Y. J.; Kang, S.; Kim, H. Y.; Gai, W. P.; Hahn, J. S.; Paik, S. R. Real-time analysis of amyloid fibril formation of alpha-synuclein using a fibrillation-state-specific fluorescent probe of JC-1. *Biochem. J.* **2009**, *418*, 311–23.

(17) Ribeiro Morais, G.; Vicente Miranda, H.; Santos, I. C.; Santos, I.; Outeiro, T. F.; Paulo, A. Synthesis and in vitro evaluation of fluorinated styryl benzazoles as amyloid-probes. *Bioorg. Med. Chem.* **2011**, *19*, 7698–710.

- (18) Watanabe, H.; Ariyoshi, T.; Ozaki, A.; Ihara, M.; Ono, M.; Saji, H. Synthesis and biological evaluation of novel radioiodinated benzimidazole derivatives for imaging alpha-synuclein aggregates. *Bioorg. Med. Chem.* **2017**, *25*, 6398–6403.
- (19) Sgourakis, N. G.; Yau, W. M.; Qiang, W. Modeling an in-register, parallel "iowa" abeta fibril structure using solid-state NMR data from labeled samples with rosetta. *Structure* **2015**, *23*, 216–27.
- (20) Dearborn, A. D.; Wall, J. S.; Cheng, N.; Heymann, J. B.; Kajava, A. V.; Varkey, J.; Langen, R.; Steven, A. C. alpha-Synuclein Amyloid Fibrils with Two Entwined, Asymmetrically Associated Protofibrils. *J. Biol. Chem.* **2016**, *291*, 2310–8.
- (21) Paxinos, G.; Watson, C. *The rat brain in stereotaxic coordinates*, 6th ed.; Academic Press, 2007; p 456.
- (22) Mougenot, A. L.; Nicot, S.; Bencsik, A.; Morignat, E.; Verchere, J.; Lakhdar, L.; Legastelois, S.; Baron, T. Prion-like acceleration of a synucleinopathy in a transgenic mouse model. *Neurobiol. Aging* **2012**, *33*, 2225–8.
- (23) Mucke, L.; Masliah, E.; Yu, G. Q.; Mallory, M.; Rockenstein, E. M.; Tatsuno, G.; Hu, K.; Kholodenko, D.; Johnson-Wood, K.; McConlogue, L. High-level neuronal expression of abeta 1–42 in wild-type human amyloid protein precursor transgenic mice: synaptotoxicity without plaque formation. *J. Neurosci.* **2000**, *20*, 4050–8.
- (24) Lancelot, S.; Roche, R.; Slimen, A.; Bouillot, C.; Levigoureux, E.; Langlois, J. B.; Zimmer, L.; Costes, N. A multi-atlas based method for automated anatomical rat brain MRI segmentation and extraction of PET activity. *PLoS One* **2014**, *9*, e109113.
- (25) Thie, J. A. Understanding the standardized uptake value, its methods, and implications for usage. *J. Nucl. Med.* **2004**, *45*, 1431–1434.
- (26) Verdurand, M.; Chauveau, F.; Daoust, A.; Morel, A. L.; Bonnefoi, F.; Liger, F.; Berod, A.; Zimmer, L. Differential effects of amyloid-beta 1–40 and 1–42 fibrils on 5-HT<sub>1A</sub> serotonin receptors in rat brain. *Neurobiol. Aging* **2016**, *40*, 11–21.
- (27) Pike, V. W. PET radiotracers: crossing the blood-brain barrier and surviving metabolism. *Trends Pharmacol. Sci.* **2009**, *30*, 431–40.
- (28) Kovacs, G. G.; Wagner, U.; Dumont, B.; Pikkarainen, M.; Osman, A. A.; Streichenberger, N.; Leisser, I.; Verchere, J.; Baron, T.; Alafuzoff, I.; Budka, H.; Perret-Liaudet, A.; Lachmann, I. An antibody with high reactivity for disease-associated alpha-synuclein reveals extensive brain pathology. *Acta Neuropathol.* **2012**, *124*, 37–50.
- (29) Peelaerts, W.; Baekelandt, V. a-Synuclein strains and the variable pathologies of synucleinopathies. *J. Neurochem.* **2016**, *139*, 256–274.
- (30) Vilar, M.; Chou, H. T.; Luhrs, T.; Maji, S. K.; Riek-Loher, D.; Verel, R.; Manning, G.; Stahlberg, H.; Riek, R. The fold of alpha-synuclein fibrils. *Proc. Natl. Acad. Sci. U. S. A.* **2008**, *105*, 8637–42.
- (31) Tuttle, M. D.; Comellas, G.; Nieuwkoop, A. J.; Covell, D. J.; Berthold, D. A.; Klopper, K. D.; Courtney, J. M.; Kim, J. K.; Barclay, A. M.; Kendall, A.; Wan, W.; Stubbs, G.; Schwieters, C. D.; Lee, V. M.; George, J. M.; Rienstra, C. M. Solid-state NMR structure of a pathogenic fibril of full-length human alpha-synuclein. *Nat. Struct. Mol. Biol.* **2016**, *23*, 409–15.
- (32) Balamurugan, K.; Murugan, N. A.; Agren, H. Multistep Modeling Strategy To Improve the Binding Affinity Prediction of PET Tracers to Abeta42: Case Study with Styrylbenzoxazole Derivatives. *ACS Chem. Neurosci.* **2016**, *7*, 1698–1705.
- (33) Poncin-Epaillard, F.; Mille, C.; Debarnot, D.; Zorzi, W.; El Moualij, B.; Coudreuse, A.; Legeay, G.; Quadrio, I.; Perret-Liaudet, A. Study of the adhesion of neurodegenerative proteins on plasma-modified and coated polypropylene surfaces. *J. Biomater. Sci., Polym. Ed.* **2012**, *23*, 1879–1893.
- (34) Vrlinic, T.; Debarnot, D.; Legeay, G.; Coudreuse, A.; El Moualij, B.; Zorzi, W.; Perret-Liaudet, A.; Quadrio, I.; Mozetic, M.; Poncin-Epaillard, F. Are the interactions between recombinant prion proteins and polymeric surfaces related to the hydrophilic/hydrophobic balance? *Macromol. Biosci.* **2012**, *12*, 830–9.
- (35) Bousset, L.; Pieri, L.; Ruiz-Arlandis, G.; Gath, J.; Jensen, P. H.; Habenstein, B.; Madiona, K.; Olieric, V.; Bockmann, A.; Meier, B. H.; Melki, R. Structural and functional characterization of two alpha-synuclein strains. *Nat. Commun.* **2013**, *4*, 2575.
- (36) Petkova, A. T.; Leapman, R. D.; Guo, Z.; Yau, W. M.; Mattson, M. P.; Tycko, R. Self-propagating, molecular-level polymorphism in Alzheimer's beta-amyloid fibrils. *Science* **2005**, *307*, 262–265.
- (37) Prusiner, S. B.; Woerman, A. L.; Mordes, D. A.; Watts, J. C.; Rampersaud, R.; Berry, D. B.; Patel, S.; Oehler, A.; Lowe, J. K.; Kravitz, S. N.; Geschwind, D. H.; Glidden, D. V.; Halliday, G. M.; Middleton, L. T.; Gentleman, S. M.; Grinberg, L. T.; Giles, K. Evidence for alpha-synuclein prions causing multiple system atrophy in humans with parkinsonism. *Proc. Natl. Acad. Sci. U. S. A.* **2015**, *112*, E5308–17.
- (38) Kherlopian, A. R.; Song, T.; Duan, Q.; Neimark, M. A.; Po, M. J.; Gohagan, J. K.; Laine, A. F. A review of imaging techniques for systems biology. *BMC Syst. Biol.* **2008**, *2*, 74.
- (39) Johnstrom, P.; Bird, J. L.; Davenport, A. P. Quantitative phosphor imaging autoradiography of radioligands for positron emission tomography. *Methods Mol. Biol.* **2012**, *897*, 205–20.
- (40) Maeda, J.; Ji, B.; Irie, T.; Tomiyama, T.; Maruyama, M.; Okauchi, T.; Staufienbiel, M.; Iwata, N.; Ono, M.; Saido, T. C.; Suzuki, K.; Mori, H.; Higuchi, M.; Suhara, T. Longitudinal, quantitative assessment of amyloid, neuroinflammation, and anti-amyloid treatment in a living mouse model of Alzheimer's disease enabled by positron emission tomography. *J. Neurosci.* **2007**, *27*, 10957–68.
- (41) Klunk, W. E.; Lopresti, B. J.; Ikonovic, M. D.; Lefterov, I. M.; Koldamova, R. P.; Abrahamson, E. E.; Debnath, M. L.; Holt, D. P.; Huang, G. F.; Shao, L.; DeKosky, S. T.; Price, J. C.; Mathis, C. A. Binding of the positron emission tomography tracer Pittsburgh compound-B reflects the amount of amyloid-beta in Alzheimer's disease brain but not in transgenic mouse brain. *J. Neurosci.* **2005**, *25*, 10598–10606.
- (42) Toyama, H.; Ye, D.; Ichise, M.; Liow, J. S.; Cai, L.; Jacobowitz, D.; Musachio, J. L.; Hong, J.; Crescenzo, M.; Tipre, D.; Lu, J. Q.; Zoghbi, S.; Vines, D. C.; Seidel, J.; Katada, K.; Green, M. V.; Pike, V. W.; Cohen, R. M.; Innis, R. B. PET imaging of brain with the beta-amyloid probe, [<sup>11</sup>C]6-OH-BTA-1, in a transgenic mouse model of Alzheimer's disease. *Eur. J. Nucl. Med. Mol. Imaging* **2005**, *32*, 593–600.
- (43) Furumoto, S.; Okamura, N.; Iwata, R.; Yanai, K.; Arai, H.; Kudo, Y. Recent advances in the development of amyloid imaging agents. *Curr. Top. Med. Chem.* **2007**, *7*, 1773–89.
- (44) Okamura, N.; Suemoto, T.; Shimadzu, H.; Suzuki, M.; Shiomitsu, T.; Akatsu, H.; Yamamoto, T.; Staufienbiel, M.; Yanai, K.; Arai, H.; Sasaki, H.; Kudo, Y.; Sawada, T. Styrylbenzoxazole derivatives for in vivo imaging of amyloid plaques in the brain. *J. Neurosci.* **2004**, *24*, 2535–2541.
- (45) Levigoureux, E.; Lancelot, S.; Bouillot, C.; Chauveau, F.; Verdurand, M.; Verchere, J.; Billard, T.; Baron, T.; Zimmer, L. Binding of the PET radiotracer [(1)(8)F]BF227 does not reflect the presence of alpha-synuclein aggregates in transgenic mice. *Curr. Alzheimer Res.* **2014**, *11*, 955–60.
- (46) Zimmer, L.; Luxen, A. PET radiotracers for molecular imaging in the brain: past, present and future. *NeuroImage* **2012**, *61*, 363–70.
- (47) Irvine, G. B.; El-Agnaf, O. M.; Shankar, G. M.; Walsh, D. M. Protein aggregation in the brain: the molecular basis for Alzheimer's and Parkinson's diseases. *Mol. Med.* **2008**, *14*, 451–464.
- (48) Anderson, V. L.; Webb, W. W. Transmission electron microscopy characterization of fluorescently labelled amyloid beta 1–40 and alpha-synuclein aggregates. *BMC Biotechnol.* **2011**, *11*, 125.
- (49) Seidel, K.; Mahlke, J.; Siswanto, S.; Kruger, R.; Heinsen, H.; Auburger, G.; Bouzrou, M.; Grinberg, L. T.; Wicht, H.; Korf, H. W.; den Dunnen, W.; Rub, U. The brainstem pathologies of Parkinson's disease and dementia with Lewy bodies. *Brain Pathol.* **2015**, *25*, 121–35.
- (50) Cykowski, M. D.; Coon, E. A.; Powell, S. Z.; Jenkins, S. M.; Benarroch, E. E.; Low, P. A.; Schmeichel, A. M.; Parisi, J. E. Expanding the spectrum of neuronal pathology in multiple system atrophy. *Brain* **2015**, *138*, 2293–309.

(51) Fodero-Tavoletti, M. T.; Smith, D. P.; McLean, C. A.; Adlard, P. A.; Barnham, K. J.; Foster, L. E.; Leone, L.; Perez, K.; Cortes, M.; Culvenor, J. G.; Li, Q. X.; Laughton, K. M.; Rowe, C. C.; Masters, C. L.; Cappai, R.; Villemagne, V. L. In vitro characterization of Pittsburgh compound-B binding to Lewy bodies. *J. Neurosci.* **2007**, *27*, 10365–71.

(52) Choi, S. R.; Schneider, J. A.; Bennett, D. A.; Beach, T. G.; Bedell, B. J.; Zehntner, S. P.; Krautkramer, M. J.; Kung, H. F.; Skovronsky, D. M.; Hefti, F.; Clark, C. M. Correlation of amyloid PET ligand florbetapir F 18 binding with Abeta aggregation and neuritic plaque deposition in postmortem brain tissue. *Alzheimer Dis. Assoc. Disord.* **2012**, *26*, 8–16.

(53) Ikonomic, M. D.; Klunk, W. E.; Abrahamson, E. E.; Mathis, C. A.; Price, J. C.; Tsopelas, N. D.; Lopresti, B. J.; Ziolk, S.; Bi, W.; Paljug, W. R.; Debnath, M. L.; Hope, C. E.; Isanski, B. A.; Hamilton, R. L.; DeKosky, S. T. Post-mortem correlates of in vivo PiB-PET amyloid imaging in a typical case of Alzheimer's disease. *Brain* **2008**, *131*, 1630–45.